

See discussions, stats, and author profiles for this publication at: <https://www.researchgate.net/publication/221728695>

# Lateral Etching of Core-Shell Au@Metal Nanorods to Metal-Tipped Au Nanorods with Improved Catalytic Activity

ARTICLE *in* ACS NANO · FEBRUARY 2012

Impact Factor: 12.88 · DOI: 10.1021/nn203793k · Source: PubMed

---

CITATIONS

62

---

READS

19

5 AUTHORS, INCLUDING:



Xia Guo

Shandong University

9 PUBLICATIONS 134 CITATIONS

SEE PROFILE

# Lateral Etching of Core–Shell Au@Metal Nanorods to Metal-Tipped Au Nanorods with Improved Catalytic Activity

Xia Guo,<sup>†</sup> Qiao Zhang,<sup>†</sup> Yanghui Sun,<sup>‡</sup> Qing Zhao,<sup>‡</sup> and Jian Yang<sup>†,§,\*</sup>

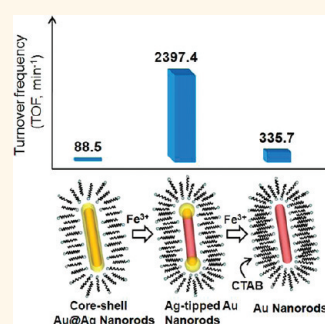
<sup>†</sup>School of Chemistry and Chemical Engineering, South China University of Technology, Guangzhou 510640, People's Republic of China, <sup>‡</sup>State Key Laboratory for Mesoscopic Physics, and Electron Microscopy Laboratory, Department of Physics, Peking University, Beijing 100871, People's Republic of China, and <sup>§</sup>School of Chemistry and Chemical Engineering, Shandong University, Jinan 250100, People's Republic of China

Efficient organization of different building blocks into well-defined nanostructures has attracted extensive attention, due to diverse organization modes, tunable physical properties, and great application potential.<sup>1–8</sup> However, the small size of the building blocks on the order of nanometers brings about huge challenges for this assembly. After great efforts have been devoted to this field for years, remarkable progress has been made, particularly in the formation of dumbbell-like nanocrystals where different building blocks are located in a linear alignment.<sup>9–11</sup> Up to date, the dumbbell-like nanohybrids are usually achieved by the selective growth of a second-component material at the ends of nanorods. This selective growth originates from the high reactivity of the crystal facets at the ends of the nanorods, which might be caused by less surface passivation, high-index crystal facets, and/or large surface curvature.<sup>1–3</sup> This growth strategy has been applied for a variety of dumbbell-like nanohybrids, such as Ag-tipped Au nanorods,<sup>12–14</sup> ZnSe-tipped CdS nanorods,<sup>15</sup> Bi<sub>2</sub>Te<sub>3</sub>-tipped Te nanorods,<sup>16</sup> etc. However, the selective growth always necessitates special seeds, complex surfactants, and strict experiment conditions. Otherwise, the growth control will be lost in the product. For example, the selective growth of silver at the ends of the gold nanorods needs multiply twinned gold nanorods as a seed.<sup>12</sup> Meanwhile, this synthetic route was conducted at a reaction temperature as high as 260 °C, resulting in the average diameter and length of the dumbbell-like nanorods with sizes of hundreds of nanometers. This size is too large for many applications. The similar selective

**ABSTRACT** Selective growth/etching of hybrid materials is very important for the rational synthesis of hierarchical structures and precise modulation of their physical properties. Here, the lateral etching of the core–shell Au@Ag nanorods is achieved by FeCl<sub>3</sub> at room temperature, producing a number of dumbbell-like Ag-tipped Au nanorods. This selective etching at the side of the core–shell nanorods is attributed to

the increased reactivity of the side facets, due to less surface passivation of cetyltrimethylammonium bromide. The similar synthetic strategy has also been demonstrated to be successful for the Pd-tipped Au nanorods that have not been reported before, indicating the great potential of this selective etching. The Ag-tipped Au nanorods are examined as a catalyst for the reduction of *p*-nitrophenol at room temperature. The Ag-tipped Au nanorods exhibit a higher catalytic activity than Au nanorods and core–shell Au@Ag nanorods, which could be attributed to the electronic effect and the unique structure in the Ag-tipped Au nanorods.

**KEYWORDS:** hybrid materials · nanostructures · reaction mechanism · selective etching · catalysis



growth could be also achieved at room temperature, based on the mixture of cetyltrimethylammonium bromide (CTAB) and benzyldimethylhexadecylammonium chloride (BDAC).<sup>13</sup> Only the presence of CTAB in the solution resulted in the increase of both diameter and length of the nanorods,<sup>14</sup> losing the growth control in the product. Meanwhile, this low-temperature route did not work for the thick gold nanorods (*d* > 15 nm).

Compared with the selective growth, the preferential etching for the dumbbell-like nanohybrids is not reported yet, although it is regarded as a powerful approach to crystal engineering of the complicated

\* Address correspondence to yangjian@scut.edu.cn.

Received for review October 4, 2011 and accepted January 8, 2012.

Published online January 08, 2012  
10.1021/nn203793k

© 2012 American Chemical Society

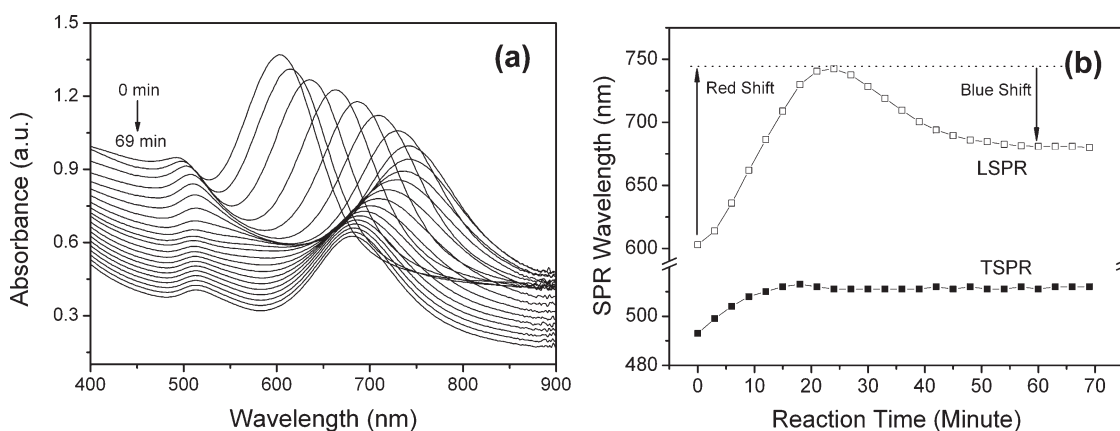


**Figure 1.** (a) UV-vis absorption spectra of the solution in which Au@Ag core-shell nanorods reacted with 25  $\mu\text{L}$  of 10 mM  $\text{FeCl}_3$ . The absorption spectra were measured at a regular interval. (b) Temporal evolution of the SPR peak positions (longitudinal surface plasmon resonance, LSPR, and transverse surface plasmon resonance, TSPR) during the reaction.

nanostructures. So far, the preferential etching about one-dimensional nanostructures is concentrated on the single-component and simple-structure systems.<sup>17–20</sup> Wang and co-workers reported the preferential etching of the gold nanorods by oxygen at an elevated temperature.<sup>18</sup> During this course, the length of the gold nanorods was shortened significantly and the diameter was kept almost the same. This result indicates that the oxidation of metallic gold substantially happens at the tip of the nanorods. The similar preferential etching of the gold nanorods was also achieved either by oxygen in the presence of  $\text{Cu}^{2+}$  and ascorbic acid or by  $\text{Fe}^{3+}$  in the presence of CTAB.<sup>19,20</sup> Recently,  $\text{Ag}_2\text{O}$ -tipped gold nanorods were used for the chemical etching. Since the inert  $\text{Ag}_2\text{O}$  particles blocked the nanorod tips, the chemical etching was limited to the side of the nanorods, resulting in some dimples on the surface.<sup>17</sup>

Here, the chemical etching of core-shell nanorods is reported for the first time. The difference of the core and shell in reactivity and their rod-like morphology offer a variety of opportunities for novel hybrid structures and unexpected properties. The selection of core-shell Au@Ag nanorods for the chemical etching is due to their easy synthesis and well-reported optical properties. Different from the case of gold nanorods, the chemical etching of the core-shell Au@Ag nanorods starts from the side, resulting in the formation of dumbbell-like Ag-tipped Au nanorods. This preferential etching to the dumbbell-like nanorods has not been reported before, to the best of our knowledge. The dumbbell-like nanorods are carefully investigated by UV-vis absorption spectroscopy, TEM microscopy, and XPS spectroscopy. Then, a reasonable mechanism is proposed for the preferential etching, which is confirmed by a series of well-designed control experiments. The preferential etching has been successfully extended for other metal-tipped gold nanorods that have not been synthesized by the selective growth. The dumbbell-like Ag-tipped Au nanorods are

demonstrated to be an excellent catalyst for the reduction of *p*-nitrophenol at room temperature, much better than the gold nanorods and the core-shell nanorods.

## RESULTS AND DISCUSSION

Figure 1a shows the absorption spectra of Au@Ag core-shell nanorods reacted with  $\text{FeCl}_3$  in the presence of CTAB. Before the addition of  $\text{FeCl}_3$ , there are two absorption peaks at 493 and 600 nm in the UV-vis absorption spectra, which can be attributed to transverse surface plasmon resonance (TSPR) and longitudinal surface plasmon resonance (LSPR) of the core-shell Au@Ag nanorods, respectively.

Compared with the TSPR and LSPR peaks of the gold nanorods at the core (TSPR = 510 nm and LSPR = 675 nm), those of the core-shell nanorods exhibit the obvious blue shifts that can be assigned to the changes of the aspect ratio and the local dielectric constant induced by surface coating.<sup>14,21</sup> After the addition of  $\text{FeCl}_3$ , the TSPR and LSPR peaks are still kept in the UV-vis absorption spectra throughout the whole process, indicating the maintenance of the rod-like shape in the product. However, the peaks gradually move to the longer wavelengths first, then shift back and finally stop at the position very close to those of the gold nanorods at the core, as shown in Figure 1a,b. This complicated moving implies that some unique changes happen to the core-shell nanorods, which might be shape deformation,<sup>18–20</sup> component change,<sup>14,21</sup> anisotropic aggregation,<sup>22,23</sup> or their combinations. Since this phenomenon is more evident for the LSPR peak in comparison with that for TSPR, the later discussion about the absorption spectra is focused on the LSPR peak. Here, two points should be highlighted for the movement of the LSPR peak. First, the complicated moving of the LSPR peak generates a maximum that is far beyond the position of the LSPR peak of the original gold nanorods at the core, which provides an important clue to understand the underlying mechanism. Second, the LSPR peak always stops

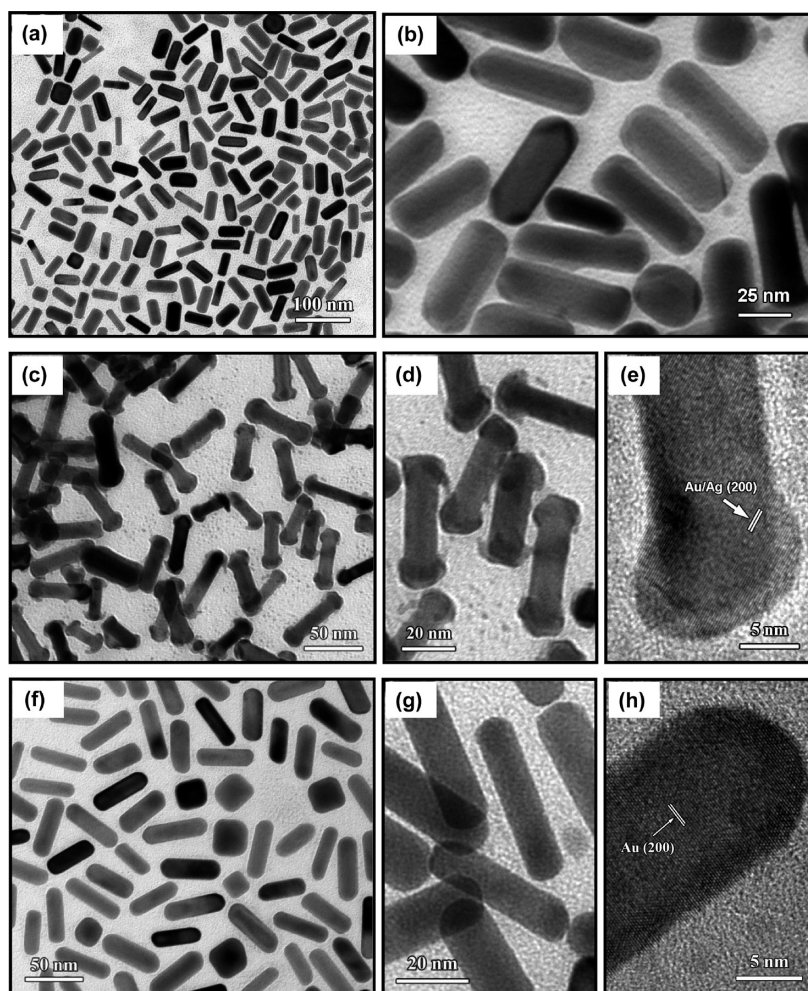


**Figure 2.** TEM and HRTEM images of Au@Ag core-shell nanorods (a,b), the etched product (c–e), and the final product when LSPR stops moving (f–h).

at the position very close to that of the original gold nanorods at the core when it moves back from the maximum. This coincidence makes it reasonable to believe that the final product could be identified as gold nanorods, which is also supported by HRTEM images and EDS spectrum. This conclusion indicates the disappearance of the silver shell at the end of this process, which well explains the intensity decrease of the LSPR peak in view of the larger absorption coefficient of silver.<sup>24</sup>

TEM microscopy was taken to check the transition of the Au@Ag core-shell nanorods induced by  $\text{FeCl}_3$  in the presence of CTAB for better understanding of the interesting shift of the LSPR peak. Figure 2a shows the TEM image of the Au@Ag core-shell nanorods before the introduction of  $\text{FeCl}_3$ . The Au@Ag core-shell nanorods exhibit a smooth surface and uniform diameter from its body to its tip. The contrast difference between the core and the shell indicates the formation of the core-shell structure in the nanorods, as presented in Figure 2b. The light shell is attributed to silver, and the dark core corresponds to gold because

gold has a higher electron density and allows fewer electrons to transmit. This result is in good agreement with the structure configuration of the core-shell Au@Ag nanorods.

Figure 2c–e shows the TEM and HRTEM images of the product when its LSPR peak moves to the maximum wavelength. The straight nanorods with the uniform diameter and smooth surface do not dominate the product any more. The resulting nanorods look like a dumbbell with two bigger tips and a thinner body. Furthermore, the tips of the dumbbell-like nanorods show the significant contrast difference (Figure 2d), which is not visualized in the body of the nanorods. EDS spectrum of the dumbbell-like nanorods (see Figure S1 in Supporting Information) shows the signals of silver and gold, besides C, Cu, and O from the copper grid. In order to clarify the distribution of Ag and Au on the nanorods, line-scanning elemental analysis along the axial direction of the nanorods is conducted for this sample. As shown in Figure S2, silver preferentially locates at the tip of the gold nanorods, which is consistent with the contrast difference

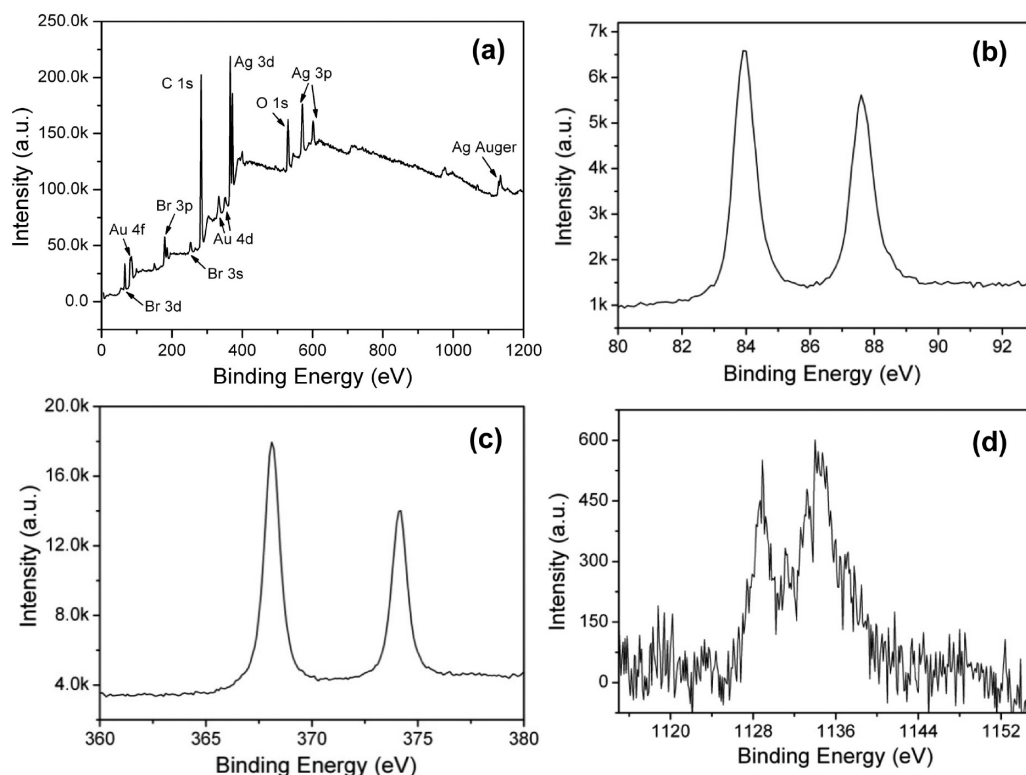


**Figure 3.** XPS spectra of the dumbbell-like Ag-tipped gold nanorods. (a) Survey spectrum, (b–d) high-resolution spectra of Au 4f, Ag 3d, Ag MVV.

observed from TEM images. Because of the similar structure and close lattice constant between gold and silver, the HRTEM image shows the clear lattice fringes throughout the whole nanorods from the tip to the body, which also implies the epitaxial growth of silver at the tip of the gold nanorods. This result directly excludes the existence of silver halide and iron hydroxide on the surface of the nanorods. So, the possibility that the red shift of the LSPR peak is caused by the formation of a new layer on the surface could be ruled out. The random dispersion and aggregation of these nanorods on the copper grid eliminates another possibility that the red shift of the LSPR peak originates from the anisotropic aggregation of the nanorods.

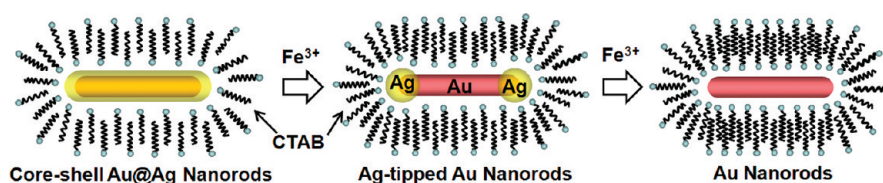
Compared with the core–shell Au@Ag nanorods at the beginning, the formation of silver-tipped gold nanorods suggests the preferential removal of the shell from the core. This transition from the core–shell nanorods to the dumbbell-like nanorods indicates the decrease of the effective diameter of the nanorod and the increase of the aspect ratio, leading to the red shift of the LSPR peak. Both results have been evidenced by statistical analysis on TEM images (see Table S1 in Supporting Information) and the shifts in UV–vis absorption spectra. Since silver only locates at the tip of the gold nanorods, the corresponding LSPR peak could be probably beyond the position of the gold nanorods at the core. Similar phenomenon was also reported for the platinum-tipped gold nanorods.<sup>25</sup> In the presence

of Ag<sup>+</sup>, platinum nanoparticles preferentially grew on the tips of the gold nanorods. This growth mode led to the obvious damping and red shift of the LSPR peak, which is attributed to the change of the shape and aspect ratio of the nanorods and the interband transition inside platinum.

Figure 2f–h shows the TEM and HRTEM images of the product when its LSPR finally stops moving. The product is dominated by the nanorods with uniform diameter and smooth surface again. The contrast difference is observed neither at the tips nor around the body of the nanorods, indicating the complete removal of the silver shell. This conclusion is also supported by the result from UV–vis absorption spectra. HRTEM images exhibit the clear lattice fringes that can be assigned to Au(200).

Figure 3 presents the typical XPS spectra of the dumbbell-like nanorods. The survey spectrum shows the presence of gold and silver in the product (Figure 3a), besides carbon, oxygen, and bromine. The signals of carbon, oxygen, and bromine are likely to come from the contamination carbon, adsorptive oxygen or CO<sub>2</sub>, and/or the surfactants attached to the surface of the nanorods. More information about the chemical component of the dumbbell-like nanorods is given by the high-resolution spectra of gold and silver. As shown in Figure 3b, the doublet at 83.9 and 87.6 eV is in good accordance with the reported data for 4f<sub>7/2</sub> and 4f<sub>5/2</sub> of elemental gold,<sup>26</sup> suggesting elemental gold in the





Scheme 1. Illustration on the possible etching mode of Au@Ag core-shell nanorods induced by  $\text{FeCl}_3$ .

product. This conclusion agrees well with those from HRTEM images and the EDS spectrum. The binding energies at 368.1 and 374.2 eV in Figure 3c can be attributed to 3d5/2 and 3d3/2 of silver.<sup>26</sup> Since the binding energies of metallic silver and its oxidative species are very close, the auger parameter of silver needs to be calculated for a clear conclusion. As illustrated in Figure 3d, the peaks located at 1128.5 and 1134.5 eV can be attributed to M4VV and M5VV transitions of silver.<sup>27</sup> The auger parameter based on the binding energy of 3d5/2 and M4VV is 726.3 eV, which is very close to that reported for elemental silver,<sup>27</sup> indicating the silver tip of the dumbbell-like nanorods is in a nature of metal.

On the basis of the above results, a reasonable reaction mechanism is proposed, as illustrated in Scheme 1. When Au@Ag core-shell nanorods are mixed with  $\text{Fe}^{3+}$  in the presence of CTAB, the silver shell could be easily oxidized into  $\text{Ag}^+$  by  $\text{Fe}^{3+}$ , as documented in the literatures.<sup>28,29</sup> The resulting silver ions react with CTAB to form a soluble complex and diffuse into the bulk solution. Since this reaction preferentially occurs on the side of the nanorods, Ag-tipped gold nanorods are produced, as evidenced by UV-vis absorption spectra, TEM, EDS, and XPS techniques. Eventually, silver would be completely removed and only the gold nanorods are left in the solution. The LSPR peak comes back from the maximum wavelength and stops at the position of the gold nanorods at the core.

This mechanism is supported by a series of well-designed control experiments. First,  $\text{Fe}(\text{NO}_3)_3$  was used in the reaction instead of  $\text{FeCl}_3$ , and the other experimental conditions were kept the same. As shown in Figure 4a, the LSPR peak in the case of  $\text{Fe}(\text{NO}_3)_3$  presented almost the same change as that of  $\text{FeCl}_3$ , indicating the importance of  $\text{Fe}^{3+}$  in the reaction. This conclusion could also be proven by a negative control experiment. In this control, NaCl was used in the reaction to replace  $\text{FeCl}_3$ . No change was observed in the absorption spectra, excluding the potential effect of  $\text{Cl}^-$  on the reaction. Second,  $\text{H}_2\text{O}_2$  was used for the reaction rather than  $\text{FeCl}_3$  to check if the other oxidative reagents also work through the process. A similar phenomenon was observed in Figure 4b, but the kinetics differed a lot from the case of  $\text{FeCl}_3$ . This difference might come from their differences in oxidizing ability. This result indicates that the role of  $\text{Fe}^{3+}$  in this reaction can be regarded as a simple oxidative reagent. On the basis of this conclusion, the shift of the

LSPR peak would become faster with an increase of  $\text{FeCl}_3$  because it effectively promotes the oxidation of the silver shell. This speculation was confirmed by a third control experiment, in which the concentration effect of  $\text{FeCl}_3$  on the reaction was studied. As shown in Figure 4c, the shift of the LSPR peak was indeed faster as the amount of  $\text{FeCl}_3$  increased. Meanwhile, it was noticed that the LSPR peak treated with different amounts of  $\text{FeCl}_3$  exhibited a close maximum wavelength, indicating that the red shift maximum is not determined by  $\text{FeCl}_3$ .

A fourth control experiment was conducted to understand the underlying reason why silver halide does not appear on the surface of the nanorods, in spite of a considerable amount of halide ions such as  $\text{Cl}^-$  and  $\text{Br}^-$  in the solution. In this control experiment,  $\text{AgNO}_3$  was introduced into the solution of KBr. The solution immediately became turbid. The white precipitation disappeared, and the solution became clear and transparent if enough CTAB was added into the solution (Figure S3). In fact, the good solubility of  $\text{Ag}^+$  in excess of CTAB was already observed in the case of the preparation of gold nanorods.<sup>30–32</sup> This result well explains the absence of silver halide on the surface of the nanorods. It should be pointed out that CTAB molecules not only act as a coordinating ligand for  $\text{Ag}^+$  but also work as a surface ligand to stabilize the nanorods in the aqueous solution. In the case of the gold nanorods, CTAB molecules selectively attach to {110} and {100} facets at the side of the nanorods, lowering the reactivity of these facets. So, the growth/etching reactions always prefer the tip of the nanorods. If most CTAB molecules adsorbed on the side of the nanorods are removed, the selective stabilization of {110} and {100} facets caused by CTAB would be remarkably weakened. Therefore, the reactivity of the surface facets is mainly determined by their intrinsic surface energies. The surface energies of {111}, {100}, and {110} facets of gold crystals are 0.58, 0.66, and 0.70  $\text{J}\cdot\text{m}^{-2}$ , respectively.<sup>33,34</sup> This result implies that the {110} facets of gold crystals have highest reactivity and would preferentially participate in the chemical reaction. Since the {110} facets are mainly located on the side of the nanorods, the growth/etching reaction would preferentially happen to the side, which has been observed in the selective etching of the gold nanorods.<sup>19</sup> The similar mechanism could be used to explain the preferential etching of the core-shell Au@Ag nanorods in our case. Less attachment of the

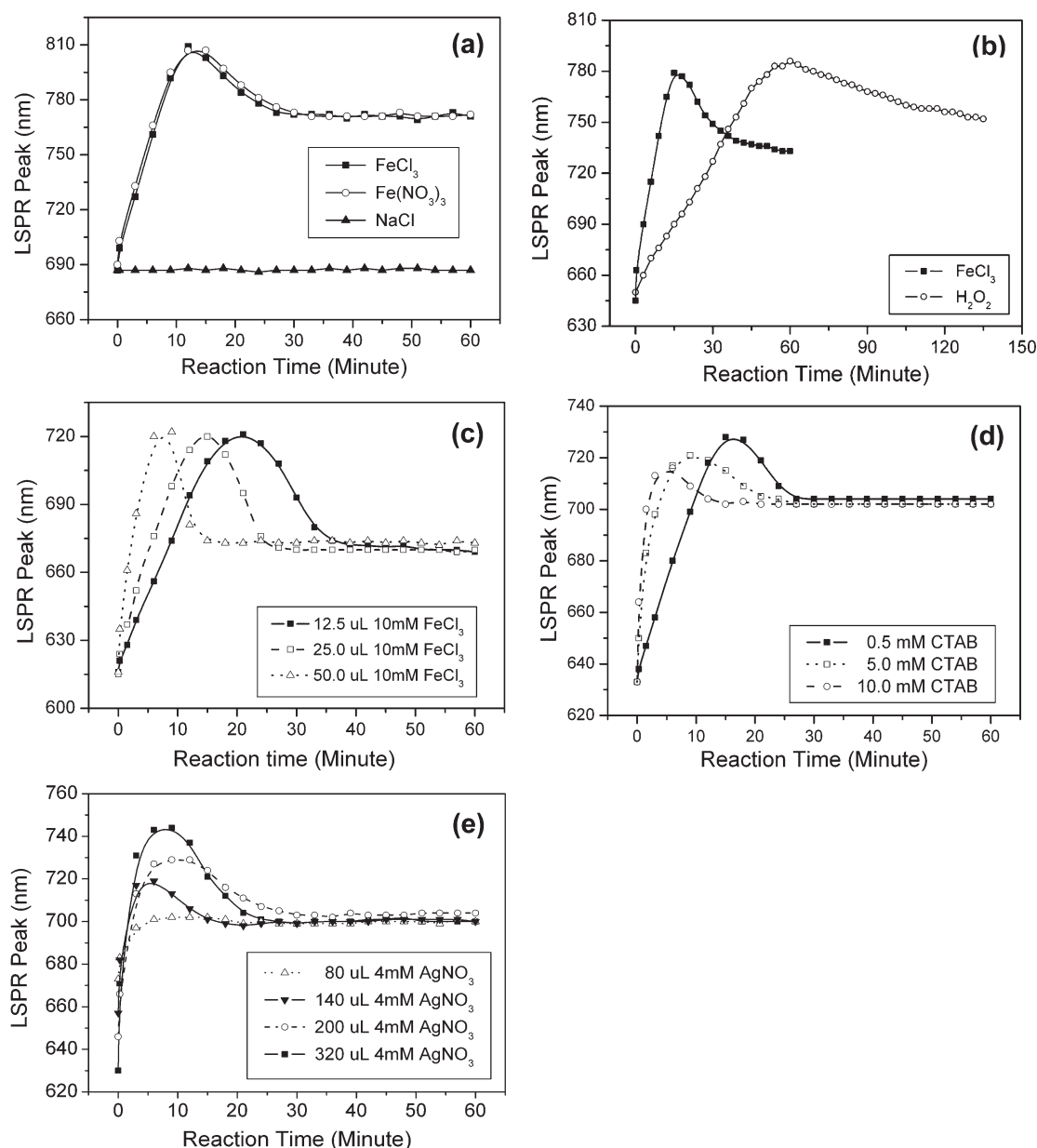


**Figure 4.** (a,b) Time dependence of the LSPR peak of the product obtained by the etching of core-shell Au@Ag nanorods with different reagents in the presence of 0.5 mM CTAB. (c,d) Time dependence of the LSPR peak of the product obtained by the etching of core-shell Au@Ag nanorods with different amounts of FeCl<sub>3</sub> or CTAB. (e) Time dependence of the LSPR peak of the product obtained by the etching of core-shell Au@Ag nanorods in different shell thicknesses. The core-shell nanorods with different shell thicknesses were prepared by using different amounts of AgNO<sub>3</sub> from the same batch of the gold nanorods.

CTAB molecules to the surface of the core-shell nanorods was supported by surface charge measurement and thermogravimetry (TG) analysis. As shown in Figure S4, the zeta-potential of the Au@Ag core-shell nanorods was only 22 mV, much lower than that of the Au nanorods at about 49 mV. This result indicates less CTAB molecules on the Au@Ag core-shell nanorods, in comparison with those on the gold nanorods. The same conclusion could also be concluded from TG analysis. The core-shell nanorods only lost 8.6% of the total weight up to 530 K, much smaller than the 31.3% for the gold nanorods (Figure S4). Less CTAB molecules

adsorbed on the core-shell nanorods could be assigned to the weak interaction between CTAB and metallic silver. So, the selective stabilization of CTAB on the different facets is greatly reduced, and the reactivity of different facets is mainly determined by the intrinsic surface energies. Therefore, the core-shell nanorods start the etching on the side. Then, the increase of the concentration of CTAB will be harmful to the formation of the dumbbell-like nanorods, which was confirmed by the following experiment. As shown in Figure 4d, the shift of the LSPR peak exhibits a similar behavior at different concentrations of CTAB. The higher

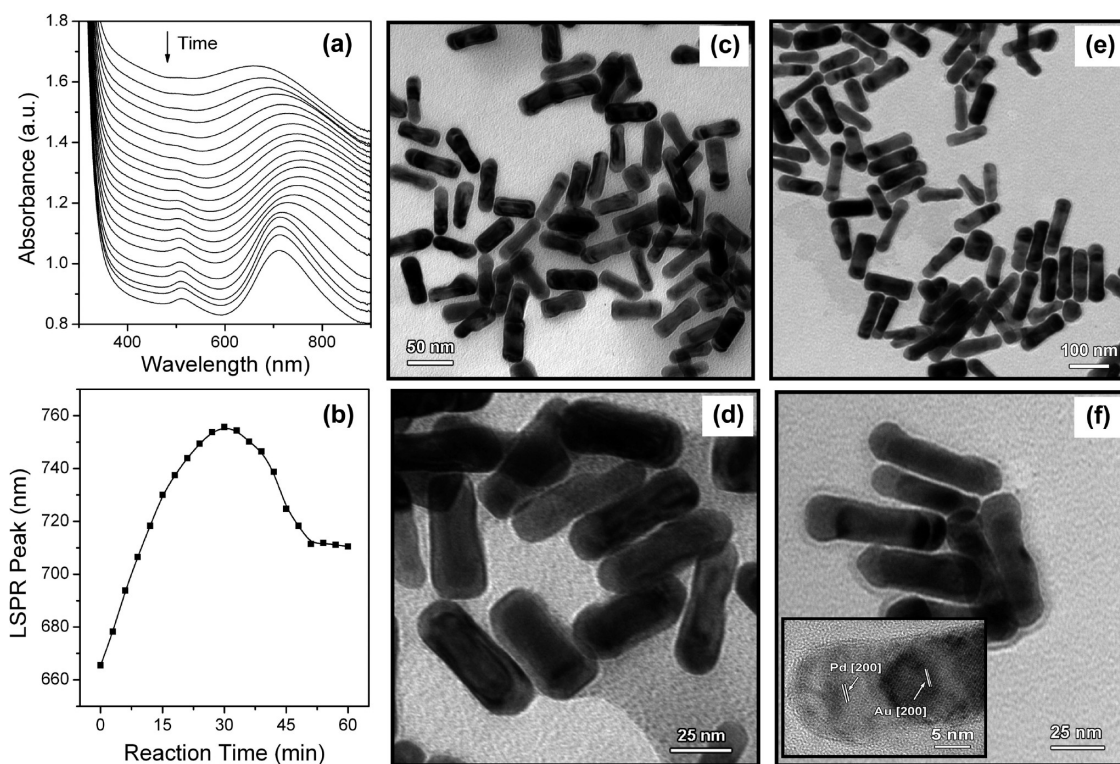


**Figure 5.** (a) UV-vis absorption spectra of the Au@Pd core-shell nanorods reacted with  $\text{H}_2\text{O}_2$  at different reaction times. (b) Dependence of the LSPR peak on the reaction time. (c,d) TEM images of the Au@Pd core-shell nanorods. (e,f) TEM images of the Pd-tipped Au nanorods. The inset in (f) is the HRTEM image of a Pd-tipped Au nanorod.

concentration of CTAB leads to the faster shift and smaller maximum wavelength. The former indicates the accelerated dissolution of the silver shell, where the coordination role of CTAB to  $\text{Ag}^+$  dominates. The latter implies the less preferential reaction on the side, where the stabilization role of CTAB on the facets strengthens. This result is in accordance with the proposed mechanism.

The shift of the LSPR peak was also affected by the thickness of the silver shell of Au@Ag core-shell nanorods, as shown in Figure 4e. The Au@Ag core-shell nanorods with the different shell thicknesses were obtained by the same procedure, and only the amount of  $\text{AgNO}_3$  varied in the reaction recipe. Since these Au@Ag nanorods were prepared from the same batch of the gold nanorods, the thickness of the silver shell could be reflected by the position of the LSPR peak in the absorption spectra.<sup>21</sup> The LSPR peak at the shorter wavelength indicates the thicker silver shell. Then, these obtained Au@Ag nanorods were treated with  $\text{FeCl}_3$  at room temperature. The thicker silver shell would produce more significant dumbbell-like nanostructures, resulting in a larger red shift of the LSPR peak. This speculation is in accordance with the experiments (Figure 4e).

This preferential etching on Au@Ag core-shell nanorods could be applied to the similar core-shell nanorods. In order to prove this point, Au@Pd core-shell nanorods are prepared by a reported method and used for the reaction.<sup>35</sup> Then,  $\text{H}_2\text{O}_2$  is taken as the

oxidizing reagent, and the pH of the solution is adjusted to 1, both of which ensure enough oxidizing ability for metallic palladium. As a result, a similar shift of the LSPR peak is observed, as presented in Figure 5a,b. The LSPR peak exhibits a huge red shift and then moves back to the position of the gold nanorods at the core. Figure 5c,d shows the TEM images of the as-obtained Au@Pd core-shell nanorods. In these nanorods, palladium is uniformly coated on the surface of the gold nanorods, reflected by the contrast difference in TEM images and the elemental identification in EDS spectrum (see Figure S5). When the LSPR peak moves to the maximum, the contrast difference between Pd and Au clearly shows the selective location of Pd at the tips of the gold nanorods (Figure 5e,f), indicating the preferential removal of the Pd shell from the side. HRTEM image clearly shows the epitaxial growth between gold and palladium. This preferential etching of the Pd shell is also supported by the change of the aspect ratio of the nanorods. As the LSPR peak reaches the maximum wavelength, the aspect ratio of the product increases to 3.33 from 2.93 of the Au@Pd core-shell nanorods (see Table S2 in Supporting Information). The increase of the aspect ratio also effectively verifies the preferential removal of the Pd shell from the body. The successful fabrication of the Pd-tipped gold nanorods confirms the potential of this strategy to other core-shell nanorods.



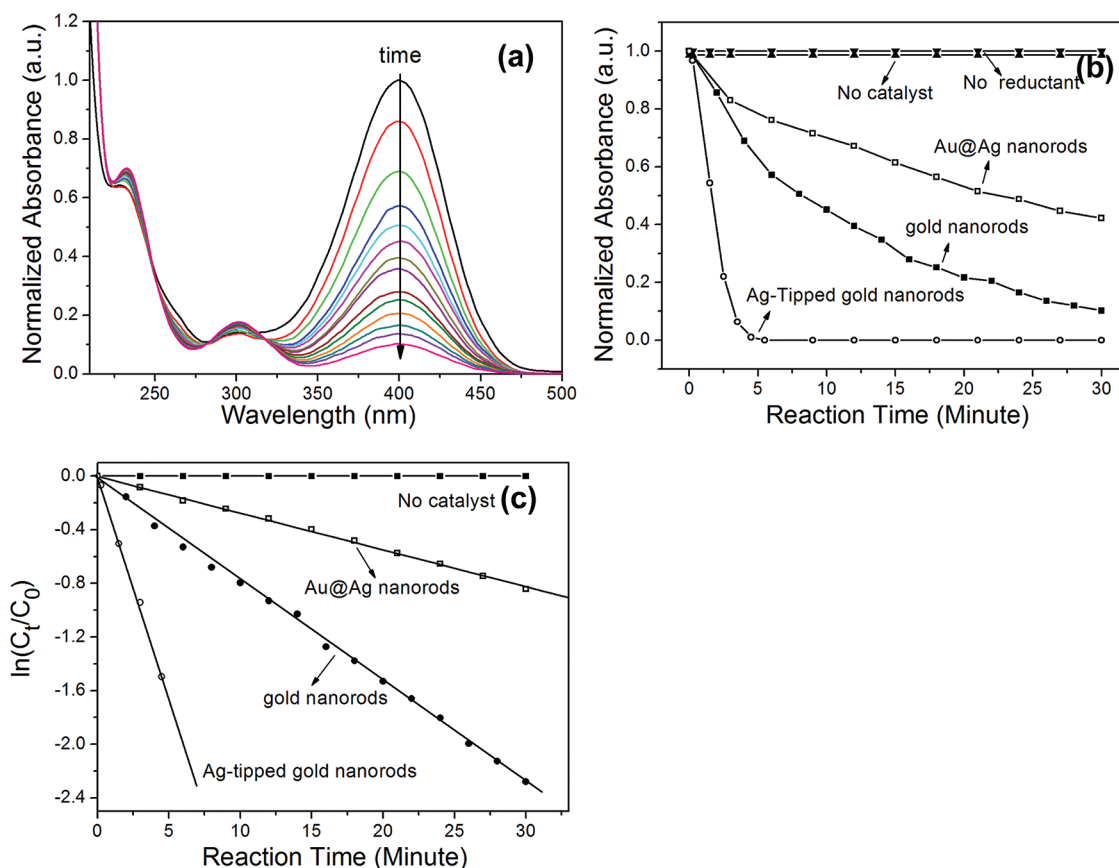


**Figure 6.** (a) Evolution of the UV–vis absorption spectra of *p*-nitrophenol reduced by NaBH<sub>4</sub> in the presence of gold nanorods. (b) Normalized absorbance of *p*-nitrophenol at 400 nm as a function of reaction time based on different nanorods as the catalyst. (c) Plots of  $\ln(C_t/C_0)$  versus reaction time for different nanorods as the catalyst.

The catalytic activities of the above nanorods are examined, using the reduction of *p*-nitrophenol to aminophenol as a model reaction. Here, aminophenol is an important intermediate for medicines, dyes, and organic synthesis. The selection of this reducing reaction could be attributed to the fact that the catalysis has been reported for gold nanoparticles.<sup>36–38</sup> Figure 6a shows the typical UV–vis absorption spectra of *p*-nitrophenol reduced by NaBH<sub>4</sub> with the gold nanorods as a catalyst. The strong absorption peak at 400 nm is the optical feature of *p*-nitrophenol. The gradual decreasing of the peak intensity indicates the successive reduction of *p*-nitrophenol. Meanwhile, the small absorption peak at 300 nm slowly increases with the reaction time, suggesting the formation of *p*-aminophenol. After 30 min, ~90% of *p*-nitrophenol was reduced, as shown in Figure 6b. Without the catalyst or the reducing agent, this reaction almost stops, suggesting that both of them are necessary for the reaction. Using the same number of the Au@Ag core–shell nanorods as the catalyst, the conversion of *p*-nitrophenol within 30 min could be approximately 58%, much lower than that of the gold nanorods. The complete conversion of *p*-nitrophenol could be finished within 4 min if the Ag-tipped Au nanorods were used as the catalyst. Because the amount of NaBH<sub>4</sub> is

far excessive for the reduction of *p*-nitrophenol, the concentration of NaBH<sub>4</sub> could be regarded as a constant throughout the whole reaction. Therefore, the rate constant can be estimated based on the pseudo-first-order kinetics.<sup>36–38</sup> As presented in the Figure 6c, the apparent rate constants of core–shell Au@Ag nanorods, Ag-tipped Au nanorods, and Au nanorods are 0.0274, 0.324, and 0.0759 min<sup>−1</sup>, respectively. These results indicate that the Ag-tipped Au nanorods show the fastest reaction rate, 4.3 times higher than that of Au nanorods and 11.8 times higher than that of core–shell Au@Ag nanorods. The improved catalytic activity of Ag-tipped Au nanorods can be attributed to the electronic effect and their unique structure. The electronic effect, also termed as “ligand effect”, can originate from the heterometallic bonding on or near the surface, which has been widely reported in a number of catalytic reactions based on bimetallic nanoparticles.<sup>39–44</sup>

Mavrikakis and Eichhorn synthesized Ru@Pt core–shell nanoparticles and studied their catalytic activity in the preferential oxidation of CO in hydrogen.<sup>42,43</sup> The core–shell nanoparticles exhibited a higher catalytic activity than the monometallic nanoparticles. The superior catalytic activity was explained by the modification of the electronic structure in the core–shell

nanoparticles. Toshima and co-workers further correlated the electronic effect with the ionization potential of metals to explain the improved catalytic activity of bimetallic nanoparticles.<sup>44,45</sup> They suggested that the electronic charge would transfer from Ag to Au, in view of the ionization potential of Au and Ag at 9.22 and 7.58 eV. This result would increase the electron density on the surface of gold, activating the dissolved oxygen for the oxidation of glucose. This kind of the charge transfer from Ag to Au was also supported by density functional theory (DFT) for Au–Ag clusters.<sup>46,47</sup> The negatively charged gold atoms are expected to be capable of activating reactions for catalysis.<sup>46</sup> It is believed that the similar mechanism also works for our catalysis, but the different arrangements of silver and gold in the catalysts greatly affect the catalytic efficiency, similar to what happens to the core–shell and alloy nanoparticles.<sup>42,43</sup> In the Ag-tipped Au nanorods, the electronic effect between gold and silver makes the electron density of gold increase and gold is directly exposed to the solution, promoting the reduction of *p*-nitrophenol. In the Au@Ag core–shell nanorods, an electron-deficient silver shell rather than the gold core is exposed to the reactants, which results in the decrease of the catalytic efficiency. This result confirms the importance of accurate control on the material arrangement in nanohybrids. On the basis of the ionization potential theory proposed by Toshima,<sup>44,48</sup> the similar effect could also occur from palladium to gold. Thus, the improved catalytic efficiency should also be expected for Pd-tipped Au nanorods, compared with pure Au nanorods. This speculation has been confirmed by the control experiment using Pd-tipped Au nanorods as a catalyst. As shown in Figure S6, the Pd-tipped Au nanorods exhibit a larger reaction rate than the gold nanorods, confirming the above mechanism again. The excellent catalytic

efficiency of the Ag-tipped Au nanorods is also supported by turnover frequencies (TOFs), defined as the numbers of *p*-nitrophenol converted by the metal atoms on the surface per minute. TOFs of core–shell Au@Ag nanorods, Au nanorods, and Ag-tipped Au nanorods are 88.5, 335.7, and 2397.4 min<sup>−1</sup>, which is also consistent with the trend from the rate constant.

## CONCLUSIONS

In summary, monodisperse Ag-tipped gold nanorods were prepared by the preferential etching of the core–shell Au@Ag nanorods with FeCl<sub>3</sub> in the presence of CTAB. Different from the gold nanorods, the side of the core–shell Au@Ag nanorods exhibits a higher reactivity than the tips in the mild oxidation of silver. The preferential etching makes the effective diameter of the resulting nanorods decrease and the aspect ratio increase. So, the corresponding LSPR peak shifts to a longer wavelength. A series of well-designed control experiments reveal the underlying mechanism of the preferential etching that might be associated with the increased reactivity of the side facets, due to less surface passivation of CTAB. The preferential etching could be extended to other core–shell nanorods, such as Au@Pd nanorods, indicating the promising potential of this preferential etching. The dumbbell-like Ag-tipped Au nanorods are examined as a catalyst in the reduction of *p*-nitrophenol at room temperature. The reaction rate based on the dumbbell-like nanorods is much higher than those of the gold nanorods and the core–shell nanorods, which could be attributed to the electronic effect between gold and silver and the unique structure of dumbbell nanorods. This result shows the great potential of the dumbbell-like nanorods in practical applications, such as catalytic reactions, ultrasensitive detection, and optoelectronic devices.

## EXPERIMENTAL SECTION

**Chemicals and Instruments.** HAuCl<sub>4</sub>·xH<sub>2</sub>O (*x* = 3–5, Au ~ 47.8%), cetyltrimethylammonium bromide (CTAB, ≥99%), and polyvinylpyrrolidone K30 (PVP K30) were obtained from July Chemical Co. Ltd. and Bio-Life Sci&Tech. Co. Ltd. in Shanghai. Palladium chloride (Pd ≥59.0%), sodium borohydride (≥96%), and *p*-nitrophenol (≥99.5%) were purchased from Sinopharm Chemical Reagent Co. Ltd. also in Shanghai. Iron(III) chloride (≥99%), iron(III) nitrate nonahydrate (≥98.5%), and silver nitrate (≥99.8%) were ordered from Kernel Chemical Reagent Co. Ltd. in Tianjin. Ascorbic acid (≥99.7%), NaOH (≥96.0%), KBr (≥99.0%), H<sub>2</sub>O<sub>2</sub> (≥30.0%), and NaCl (≥99.5%) were obtained from Guanghua Chemical Factory Co. Ltd. in Guangzhou. All of these reagents were used without any further purification.

UV–vis absorption spectra were recorded in the range of 300–900 nm at room temperature by a Hitachi U-3010 spectrophotometer. Low-magnification TEM images were acquired with a FEI Tecnai 12 transmission electron microscope at an accelerating voltage of 100 kV. High-resolution TEM (HRTEM) images were acquired on a JEOL 2010 analytical transmission electron microscope at 200 kV. The samples for TEM images

were purified by centrifugation before the observation, in order to remove the surfactants and/or the excess of the reactants. Then, the samples were dispersed in distilled water. The obtained solution was dropped on a copper grid coated with an amorphous carbon film. The X-ray photoelectron spectra (XPS) were achieved with an AXIS Ultra DLD spectrometer (Kratos Anal.), using the radiation of Al K $\alpha$  line as the excitation source. The calibration was conducted by referring the C1s signal of the contaminate carbon to the binding energy of 284.6 eV. The zeta-potentials of the gold nanorods and Au@Ag core–shell nanorods were measured by Zetasizer Nano ZS (England). The thermal stability of gold nanorods and Au@Ag core–shell nanorods was characterized by thermogravimetry differential scanning calorimetry (TG-DSC) based on NETZSCH STA449C made in Germany.

**Synthesis of Au@Ag Core–Shell Nanorods.** The high-quality gold nanorods were obtained via a typical seed-mediated growth process.<sup>30,31</sup> The obtained gold nanorods were purified by centrifugation twice at 10000 rpm for 10 min and then dispersed in 0.1 M CTAB. The gold nanorods were used as a seed for the preparation of the Au@Ag core–shell nanorods, according to the reported methods.<sup>21</sup> In brief, 264  $\mu$ L of 4 mM AgNO<sub>3</sub>,

568  $\mu$ L of 78.8 mM ascorbic acid, and 4 mL of the solution with the gold nanorods were added into 20 mL of 1 wt % PVP. After the mixture was heated to 40  $^{\circ}$ C, 1 mL of 0.1 M NaOH was added to increase the reducing ability of ascorbic acid. As a result, the color of the solution gradually changed from wine red to green within a few minutes. The solution was cooled 30 min later. Finally, the as-prepared Au@Ag core-shell nanorods were collected by centrifugation and dispersed into 4 mL of 0.5 mM CTAB for the later reaction.

**Chemical Etching of Au@Ag Core-Shell Nanorods.** Twenty-five microliters of 10 mM FeCl<sub>3</sub> was added into 2 mL of the Au@Ag core-shell nanorods in the presence of 0.5 mM CTAB at room temperature. The UV-vis absorption spectra of the solution were tracked at a regular interval to characterize the change of the optical properties of the samples. It should be pointed out that the aqueous solution of FeCl<sub>3</sub> has to be fresh. Otherwise, FeCl<sub>3</sub> would hydrolyze easily to generate hydroxides and the solution becomes turbid.

**Synthesis and Chemical Etching of Au@Pd Core-Shell Nanorods.** The Au@Pd core-shell nanorods were prepared via a typical seed-mediated growth process.<sup>35</sup> The as-obtained Au@Pd core-shell nanorods were purified by centrifugation at 11 000 rpm for 15 min and then dispersed in 10 mL of 1 mM CTAB. The chemical etching was carried out by adding 1 mL of 9.8 M H<sub>2</sub>O<sub>2</sub> at pH 1 into 1 mL of Au@Pd core-shell solution. The UV-vis absorption spectra of the solution were tracked at a regular interval to characterize the change of the optical properties of the samples.

**Catalytic Reduction of *p*-Nitrophenol.** The catalytic reduction of *p*-nitrophenol was conducted by a procedure similar to those reported in the literature.<sup>36,37</sup> First, 9 mL of 0.18 mM *p*-nitrophenol was added to 1 mL of 0.6 M ice-cold NaBH<sub>4</sub>, and the solution was vigorously stirred for 10 min at room temperature. After that, the appropriate amount of the gold-based nanorods (Au, Au@Ag, or Ag-tipped Au) was added to start the reducing reaction of *p*-nitrophenol. The reducing process of *p*-nitrophenol was monitored by measuring the absorption spectra of the solution at regular intervals.

**Acknowledgment.** This work was supported by Natural Science Foundation of China (20801019, 21071055, 21172076), New Century Excellent Talents in University (NCET-10-0369), National Basic Research Program of China (2011CB935901), Natural Science Foundation of Guangdong Province, Independent Innovation Foundation and Start-up Funding in Shandong University. The authors thank Ms. Liu and Prof. Xuan Lun at South China Agricultural University for TEM measurements, Mr. Rui Zhu at Peking University for line-scanning elemental analysis, Mr. Yujun Ge, Ms. Rong Wu, and Mr. Cheng Chi for their help in catalysis reaction, Dr. Zhenxing Liang for the valuable discussion about the catalysis reaction.

**Supporting Information Available:** EDS and the catalytic activity of the metal-tipped Au nanorods; line-scanning element analysis of a single dumbbell-like nanorod; real color photograph of the solution of AgBr with different reagents; zeta-potential and TG curves of the core-shell Au@Ag nanorods and the Au nanorods and the average size of the core-shell Au@Metal nanorods and the resulting metal-tipped Au nanorods. This material is available free of charge via the Internet at <http://pubs.acs.org>.

## REFERENCES AND NOTES

- Costi, R.; Saunders, A. E.; Banin, U. Colloidal Hybrid Nanostructures: A New Type of Functional Materials. *Angew. Chem., Int. Ed.* **2010**, *49*, 4878–4897.
- Hao, R.; Xing, R.; Xu, Z.; Hou, Y. L.; Gao, S.; Sun, S. H. Synthesis, Functionalization, and Biomedical Applications of Multifunctional Magnetic Nanoparticles. *Adv. Mater.* **2010**, *22*, 2729–2742.
- Cozzoli, P. D.; Pellegrino, T.; Manna, L. Synthesis, Properties and Perspectives of Hybrid Nanocrystal Structures. *Chem. Soc. Rev.* **2006**, *35*, 1195–1208.
- Yang, J.; Elim, H. I.; Zhang, Q.; Lee, J. Y.; Ji, W. Rational Synthesis, Self-Assembly, and Optical Properties of PbS–Au Heterogeneous Nanostructures via Preferential
- Deposition. *J. Am. Chem. Soc.* **2006**, *128*, 11921–11926.
- Huang, S. S.; Huang, J. M.; Yang, J.; Peng, J. J.; Zhang, Q. B.; Peng, F.; Wang, H. J.; Yu, H. Chemical Synthesis, Structure Characterization, and Optical Properties of Hollow PbSx–Solid Au Heterodimer Nanostructures. *Chem.—Eur. J.* **2010**, *16*, 5920–5926.
- Zhu, G. X.; Xu, Z. Controllable Growth of Semiconductor Heterostructures Mediated by Bifunctional Ag<sub>2</sub>S Nanocrystals as Catalyst or Source-Host. *J. Am. Chem. Soc.* **2011**, *133*, 148–157.
- Pang, M. L.; Hu, J. Y.; Zeng, H. C. Synthesis, Morphological Control, and Antibacterial Properties of Hollow/Solid Ag<sub>2</sub>S/Ag Heterodimers. *J. Am. Chem. Soc.* **2010**, *132*, 10771–10785.
- Zeng, J.; Huang, J.; Liu, C.; Wu, C. H.; Lin, Y.; Wang, X.; Zhang, S.; Hou, J. G.; Xia, Y. Gold-Based Hybrid Nanocrystals through Heterogeneous Nucleation and Growth. *Adv. Mater.* **2010**, *22*, 1936–1940.
- Mokari, T.; Rothenberg, E.; Popov, I.; Costi, R.; Banin, U. Selective Growth of Metal Tips onto Semiconductor Quantum Rods and Tetrapods. *Science* **2004**, *304*, 1787–1790.
- Shaviv, E.; Schubert, O.; Alves-Santos, M.; Goldoni, G.; Felice, R. D.; Vallee, F.; Fatti, N. D.; Banin, U.; Sönnichsen, C. Absorption Properties of Metal–Semiconductor Hybrid Nanoparticles. *ACS Nano* **2011**, *5*, 4712–4719.
- Camargo, P. H. C.; Xiong, Y.; Ji, L.; Zuo, J. M.; Xia, Y. N. Facile Synthesis of Tadpole-like Nanostructures Consisting of Au Heads and Pd Tails. *J. Am. Chem. Soc.* **2007**, *129*, 15452–15453.
- Seo, D.; Il Yoo, C.; Jung, J.; Song, H. Ag–Au–Ag Heterometallic Nanorods Formed through Directed Anisotropic Growth. *J. Am. Chem. Soc.* **2008**, *130*, 2940–2941.
- Park, K.; Vaia, R. A. Synthesis of Complex Au/Ag Nanorods by Controlled Overgrowth. *Adv. Mater.* **2008**, *20*, 3882–3886.
- Huang, C. C.; Yang, Z.; Chang, H. T. Synthesis of Dumbbell-Shaped Core-Shell Nanorods by Seed-Mediated Growth under Alkaline Conditions. *Langmuir* **2004**, *20*, 6089–6092.
- Kirsanova, M.; Nemchinov, A.; Hewa-Kasakarage, N. N.; Schmall, N.; Zamkov, M. Synthesis of ZnSe/CdS/ZnSe Nanobells Showing Photoinduced Charge Separation. *Chem. Mater.* **2009**, *21*, 4305–4309.
- Wang, W.; Goebel, J.; He, L.; Aloni, S.; Hu, Y.; Zhen, L.; Yin, Y. Epitaxial Growth of Shape-Controlled Bi<sub>2</sub>Te<sub>3</sub>–Te Heterogeneous Nanostructures. *J. Am. Chem. Soc.* **2010**, *132*, 17316–17324.
- Bao, Z. H.; Sun, Z. H.; Xiao, M. D.; Chen, H. J.; Tian, L. W.; Wang, J. F. Transverse Oxidation of Gold Nanorods Assisted by Selective End Capping of Silver Oxide. *J. Mater. Chem.* **2011**, *21*, 11537–11543.
- Tsung, C. K.; Kou, X.; Shi, Q.; Zhang, J.; Yeung, M. H.; Wang, J.; Stucky, G. D. Selective Shortening of Single-Crystalline Gold Nanorods by Mild Oxidation. *J. Am. Chem. Soc.* **2006**, *128*, 5352–5353.
- Sreeprasad, T. S.; Samal, A. K.; Pradeep, T. Body- or Tip-Controlled Reactivity of Gold Nanorods and Their Conversion to Particles through Other Anisotropic Structures. *Langmuir* **2007**, *23*, 9463–9471.
- Zou, R. X.; Guo, X.; Yang, J.; Li, D. D.; Peng, F.; Zhang, L.; Wang, H. J.; Yu, H. Selective Etching of Gold Nanorods by Ferric Chloride at Room Temperature. *CrystEngComm* **2009**, *11*, 2797–2803.
- Liu, M. Z.; Guyot-Sionnest, P. Synthesis and Optical Characterization of Au/Ag Core/Shell Nanorods. *J. Phys. Chem. B* **2004**, *108*, 5882–5888.
- Thomas, K. G.; Barazzouk, S.; Ipe, B. I.; Joseph, S. T. S.; Kamat, P. V. Uniaxial Plasmon Coupling through Longitudinal Self-Assembly of Gold Nanorods. *J. Phys. Chem. B* **2004**, *108*, 13066–13068.
- Grzelczak, M.; Vermant, J.; Furst, E. M.; Liz-Marzan, L. M. Directed Self-Assembly of Nanoparticles. *ACS Nano* **2010**, *4*, 3591–3605.
- Doria, G.; Larginho, M.; Dias, J. T.; Pereira, E.; Franco, R.; Baptista, P. V. Gold-Silver-Alloy Nanoprobes for One-Pot Multiplex DNA Detection. *Nanotechnology* **2010**, *21*, 255101.

25. Grzelczak, M.; Perez-Juste, J.; Rodriguez-Gonzalez, B.; Liz-Marzan, L. M. Influence of Silver Ions on the Growth Mode of Platinum on Gold Nanorods. *J. Mater. Chem.* **2006**, *16*, 3946–3951.
26. Wagner, C. D.; Riggs, W. M.; Davis, L. E.; Moulder, J. F. In *Handbook of X-ray Photoelectron Spectroscopy*; Mullenberg, G. E., Ed.; Perkin-Elmer Corporation: Eden Prairie, MN, 1979.
27. Hu, C.; Lan, Y.; Qu, J.; Hu, X.; Wang, A. Ag/AgBr/TiO<sub>2</sub> Visible Light Photocatalyst for Destruction of Azodyes and Bacteria. *J. Phys. Chem. B* **2006**, *106*, 4066–4072.
28. Bi, Y. P.; Ye, J. H. *In Situ* Oxidation Synthesis of Ag/AgCl Core–Shell Nanowires and Their Photocatalytic Properties. *Chem. Commun.* **2009**, *43*, 6551–6553.
29. Sun, Y. G. Conversion of Au Nanowires to AgCl Nanowires Decorated with Au Nanoparticles and Their Photocatalytic Activity. *J. Phys. Chem. C* **2010**, *114*, 2127–2133.
30. Nikoobakht, B.; El-Sayed, M. A. Preparation and Growth Mechanism of Gold Nanorods Using Seed-Mediated Growth Method. *Chem. Mater.* **2003**, *15*, 1957–1962.
31. Sau, T. K.; Murphy, C. J. Seeded High Yield Synthesis of Short Au Nanorods in Aqueous Solution. *Langmuir* **2004**, *20*, 6414–6420.
32. Yang, Z.; Ni, W.; Kou, X.; Zhang, S.; Sun, Z.; Sun, L. D.; Wang, J. F.; Yan, C. H. Incorporation of Gold Nanorods and Their Enhancement of Fluorescence in Mesoporous Silica Thin Films. *J. Phys. Chem. C* **2008**, *112*, 18895–18903.
33. Todd, B. D.; Lynden-Bell, R. M. Surface and Bulk Properties of Metals Modelled with Sutton–Chen Potentials. *Surf. Sci.* **1993**, *281*, 191–206.
34. Uppenbrink, J.; Johnston, R. L.; Murrell, J. N. Modelling Transition Metal Surface with Empirical Potentials. *Surf. Sci.* **1994**, *304*, 223–236.
35. Xiang, Y. J.; Wu, X. C.; Liu, D. F.; Jiang, X. Y.; Chu, W. G.; Li, Z. Y.; Ma, Y.; Zhou, W. Y.; Xie, S. S. Formation of Rectangularly Shaped Pd/Au Bimetallic Nanorods: Evidence for Competing Growth of the Pd Shell between the {110} and {100} Side Facets of Au Nanorods. *Nano Lett.* **2006**, *6*, 2290–2294.
36. Lee, J.; Park, J. C.; Song, H. A Nanoreactor Framework of a Au@SiO<sub>2</sub> Yolk/Shell Structure for Catalytic Reduction of *p*-Nitrophenol. *Adv. Mater.* **2008**, *20*, 1523–1528.
37. Khalavka, Y.; Becker, J.; Sonnichsen, C. Synthesis of Rod-Shaped Gold Nanorattles with Improved Plasmon Sensitivity and Catalytic Activity. *J. Am. Chem. Soc.* **2009**, *131*, 1871–1875.
38. Kundu, S.; Lau, S.; Liang, H. Shape-Controlled Catalysis by Cetyltrimethylammonium Bromide Terminated Gold Nanospheres, Nanorods, and Nanoprisms. *J. Phys. Chem. C* **2009**, *113*, 5150–5156.
39. Wang, D.; Li, Y. Bimetallic Nanocrystals: Liquid-Phase Synthesis and Catalytic Applications. *Adv. Mater.* **2011**, *23*, 1044–1060.
40. Demirci, U. B. Theoretical Means for Searching Bimetallic Alloys as Anode Electrocatalyst for Direct Liquid-Feed Fuel Cells. *J. Power Sources* **2007**, *173*, 11–18.
41. Venkatesan, P.; Santhanalakshmi, J. Designed Synthesis of Au/Ag/Pd Trimetallic Nanoparticle-Based Catalysts for Sonogashira Coupling Reactions. *Langmuir* **2010**, *26*, 12225–12229.
42. Alayoglu, S.; Nilekar, A. U.; Mavrikakis, M.; Eichhorn, B. Ru–Pt Core–Shell Nanoparticles for Preferential Oxidation of Carbon Monoxide in Hydrogen. *Nat. Mater.* **2008**, *7*, 333–338.
43. Nilekar, A. U.; Alayoglu, S.; Eichhorn, B.; Mavrikakis, M. Preferential CO Oxidation in Hydrogen: Reactivity of Core–Shell Nanoparticles. *J. Am. Chem. Soc.* **2010**, *132*, 7418–7428.
44. Tokonami, S.; Morita, N.; Takasaki, K.; Toshima, N. Novel Synthesis, Structure, and Oxidation Catalysis of Ag/Au Bimetallic Nanoparticles. *J. Phys. Chem. C* **2010**, *114*, 10336–10341.
45. Toshima, N.; Ito, R.; Matsushita, T.; Shiraishi, Y. Trimetallic Nanoparticles Having a Au-Core Structure. *Catal. Today* **2007**, *122*, 239–244.
46. Bonacic-Koutecky, V.; Burda, J.; Mitric, R.; Ge, M.; Zampella, G.; Fantucci, P. Density Functional Study of Structural and Electronic Properties of Bimetallic Silver–Gold Clusters: Comparison with Pure Gold and Silver Clusters. *J. Chem. Phys.* **2002**, *117*, 3120–3131.
47. Lee, H. M.; Ge, M.; Sahu, B. R.; Tarakeshwar, P.; Kim, K. S. Geometrical and Electronic Structures of Gold, Silver, and Gold–Silver Binary Clusters: Origins of Ductility of Gold and Gold–Silver Alloy Formation. *J. Phys. Chem. B* **2003**, *107*, 9994–10005.
48. Moseler, M.; Hakkinen, H.; Barnett, R. N.; Landman, U. Structure and Magnetism of Neutral and Anion Palladium Clusters. *Phys. Rev. Lett.* **2001**, *86*, 2545–2548.